Chemical Geology 634 (2023) 121581

Contents lists available at ScienceDirect

Chemical Geology

journal homepage: www.elsevier.com/locate/chemgeo

Uranium uptake by phosphate minerals at hydrothermal conditions

Ángel Jiménez-Arroyo [a,*], Rinat Gabitov [a], Artas Migdisov [e], Juejing Lui [c], Andrew Strzelecki [c,e], Xiaodong Zhao [c], Xiaofeng Guo [c], Varun Paul [a], Todd Mlsna [b], Alberto Perez-Huerta [d], Florie Caporuscio [e], Hongwu Xu [e], Robert Roback [e]

[a] Department of Geosciences, Mississippi State University, United States of America
[b] Department of Chemistry, Mississippi State University, United States of America
[c] Department of Chemistry, Washington State University, United States of America
[d] Department of Geological Sciences, The University of Alabama, United States of America
[e] Earth and Environmental Sciences Division, Los Alamos National Laboratory, United States of America

ARTICLE INFO

Editor: Karen Johannesson

Keywords:
Brushite
Apatite
Uranium uptake
Partition coefficient

ABSTRACT

The goal of this work was to evaluate the immobilization of uranium (U) through crystallization of calcium phosphate minerals (phosphates), which have a strong ability to absorb and retain dissolved uranyl, and therefore, are useful in various geological and environmental applications. To date, most of the experimental studies have been conducted at room temperature and high temperature assessments on uranium immobilization rely on the extrapolation procedure, which is not always accurate. To evaluate uranium partition coefficients between phosphates and hydrothermal fluid, we performed a series of crystallization experiments at 25–350 °C and various aqueous uranium concentrations.

Crystallization occurred through the transformation of brushite to monetite or/and apatite in aqueous solutions doped with uranium aliquots. Solid products were extracted and characterized with X-ray diffraction (XRD) and scanning electron microscopy (SEM). The local bonding environment and valence state of uranium in apatite were determined via X-ray absorption spectroscopy (XAS). Uranium concentration in crystals and coexisting solutions were measured with inductively coupled plasma mass spectrometry (ICP-MS). Apparent partition coefficients were calculated as Nernst partition coefficients (D^U) and Doener-Hoskins partition coefficients ($K_{D-H}^{U/Ca}$) (to account for closed reservoir effect). Experimental D^U values were compared with those calculated using the lattice strain model. Results showed that >92% of U added to solutions was extracted via this crystallization method and $K_{D-H}^{U/Ca}$ decreases with increasing phosphate crystallization temperature. Thus, phosphates, especially apatite, has a strong potential to immobilize uranium under hydrothermal conditions and can be used in the development of engineering barriers to further improve the efficiency of existing backfill materials in the disposal of nuclear waste.

1. Introduction

The knowledge of the behavior of radionuclides in natural waters is a key factor in assessing contamination risks resulting from U mining and milling, accidents in nuclear power plants (e.g., Fukushima 2011), and waste repository sites. Moreover, there is an urgency for the development of a safe, cost-effective way to dispose of this nuclear waste. Phosphate minerals have been shown to be promising host repositories for enhancing the immobilization of radionuclides (Hughes, 2015; Rigali et al., 2016). Calcium phosphates such as brushite, monetite, apatite, and their varieties are widely known not only for being abundant but also, for their versatility (Hughes and Rakovan, 2002; Hughes, 2015; Rigali et al., 2016). For example, apatite is used for rock age determination, as a soil fertilizer, and in environmental remediation (Chew and Spikings, 2015; Hughes, 2015). In environmental remediation, apatite can be used as a permeable reactive barrier (PRBs), as a phosphate-induced metal stabilization (PIMS), or as a potential waste form phase for the immobilization of radionuclides, a wide range of water contaminants, and metals (Carpéna et al., 1997; Soulet et al., 2001; Ewing and Wang, 2002; Wright and Conca, 2002; Hughes, 2015; Rigali et al.,

* Corresponding author.
E-mail address: alj508@msstate.edu (Á. Jiménez-Arroyo).

https://doi.org/10.1016/j.chemgeo.2023.121581
Received 13 January 2023; Received in revised form 23 May 2023; Accepted 31 May 2023
Available online 5 June 2023

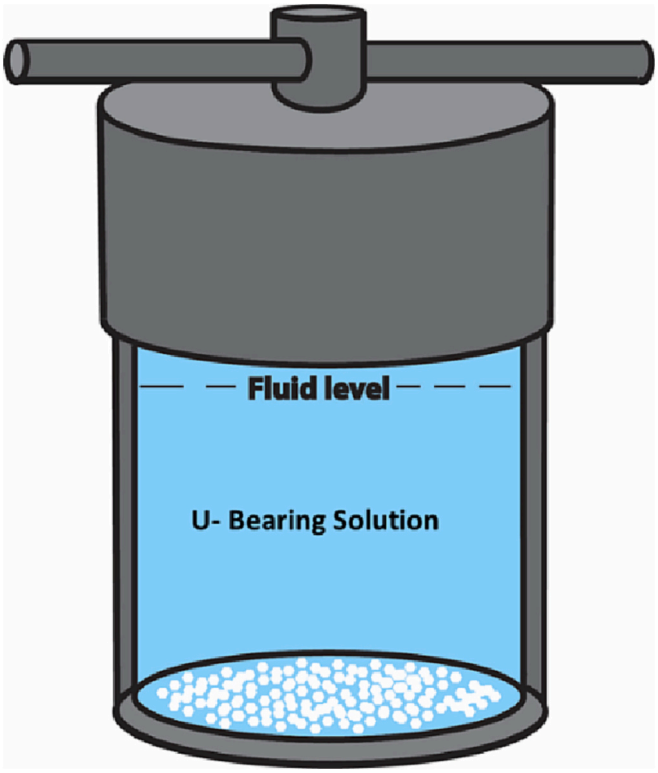

Fig. 1. Experimental setup for brushite to apatite recrystallization. U was added via the addition of U aliquots.

2016). Apatite is known to have a high affinity for the absorption of radionuclides, such as uranium, and it is not only stable at hydrothermal conditions but also in near-surface environments (Carpéna et al., 1997; Soulet et al., 2001; Chaumont et al., 2002; Hughes and Rakovan, 2002; Rigali et al., 2016). Surface adsorption is common at low temperatures, but at high temperature crystallization rate is high and therefore, nuclides can be trapped into crystal lattices. Once radionuclides are fixed into the crystal structures of phosphate minerals, they can remain isolated for hundreds of thousands to million years (Jerden and Sinha, 2003; Gorman-Lewis et al., 2009; Horie et al., 2008; Rigali et al., 2016). This idea becomes attractive since incorporating uranium and other radionuclides into low solubility solid phases represents a more efficient, cost-effective, and less invasive environmental remediation strategy (Gorman-Lewis et al., 2009; Horie et al., 2008; Rigali et al., 2016).

In nature, U is commonly found in oxidized form as $U^{6+}$and in reduced form as U^{4+}. It is established in the literature that U in its oxidized state is mobile in aqueous solutions while its reduced state is immobile (Hoeve and Sibbald, 1978; Romberger, 1984; Jefferson et al., 2007). However, recent studies have demonstrated that U^{4+} can be mobilized (up to 1 ppm) at elevated temperatures (200–350 °C) under low pH and neutral pH using NaCl and Na_2SO_4 solutions, respectively (Timofeev et al., 2018; Migdisov et al., 2019). Although U incorporation into the crystal structures of phosphate minerals has been extensively studied, those investigations are limited to ambient conditions, uranium-contaminated soils, and mineral surface ion exchange. The thermal peak of nuclear waste canisters can be up to 300 °C (Greenburg and Wen, 2013). However, U incorporation by phosphate minerals at elevated temperatures (>25 °C) remains poorly investigated., It is imperative that U entrapment by phosphate minerals at elevated temperatures is evaluated to shed light into the potential usage of phosphate minerals as an engineer barrier system. Thus, this is the goal of this study, to evaluate U entrapment at temperatures >25 °C.

2. Methodology

2.1. Experimental setup

The brushite precipitation method was modified from Moreno and Varughese (1981). The initial solutions were acquired by the dissolution of 62.39 g of calcium chloride dihydrate [$CaCl_2 \cdot 2H_2O$] and 34.76 g of sodium phosphate monobasic monohydrate [$NaH_2PO_4 \cdot H_2O$] into reverse osmosis (RO) water. Each solute was separately placed into a 500 ml beaker. To both beakers, 400 ml of RO water was added, and both beakers were placed on a magnetic stirrer for approximately 15 min to dissolve the solute entirely to form an initial solution of 1.06 M of $CaCl_2 \cdot 2H_2O$ and 0.63 M of $NaH_2PO_4 \cdot H_2O$. Once the solutes were dissolved, both solutions were poured into a 900 ml plastic container. The solution was stirred at room temperature with a Teflon coated stir bar operated by magnetic stirrer and was left for 2 days, to enable nucleation and growth of brushite crystals. After 2 days, the precipitated phosphate mineral was filtered, collected, and left to dry at room temperature.

Teflon-lined hydrothermal steel autoclaves were used to achieve brushite to apatite recrystallization. A total of 67 experiments were conducted using U aliquots. Approximately 0.2 g of brushite powder was placed at the bottom of the autoclave (autoclave volume: 100 ml; 50 ml; 15 ml) together with a 0.5 M NaCl solution (Fisher Scientific, A.C·S) (Fig. 1). The amount of solution added was set to occupy approximately 60% of the total autoclave volume. After placing these materials, aliquots of 1000 ppm U standard solution were introduced to our system to make total concentrations ranging from 0.01 to 10 ppm. The autoclaves were then sealed and loaded into a furnace preheated to 80, 120, 160, 200, 220 and 350 °C. Six autoclave experiments were conducted at room temperature (i.e., 25 °C). Three experiments were performed in large plastic containers with continues stirring of growth media using submersible magnetic stir plate at 400 rpm. Temperature was controlled by the water circulating bath at 39 °C. Experimental conditions are listed in Table 1.

2.2. Sample characterization

The solid experimental products were analyzed with X-Ray Diffraction (XRD) and Scanning Electron Microscopy (SEM) at Mississippi State University (MSU). XRD analysis was conducted using a Rigaku Ultima III X-Ray Diffraction System. MDI Jade 2010 software was used for data analysis and interpretations. The powder sample was mounted on a sample holder and loaded into the instrument. XRD runs were performed from 10 to 50° 2θ at a velocity of 4°/min and a sampling interval of 0.02°. SEM imaging was used to analyze solids to determine the morphology of the mineral phases. The powder was placed on a sample mount containing carbon tape. After placing the powder on the mount, the sample was coated with platinum shielding a 10 μm thickness. Uranium L3-edge X-ray absorption spectroscopy (XAS), including both near-edge region X-ray absorption near edge structure (XANES) and extended region X-ray absorption fine structure (XAFS), was conducted at the Advanced Photon Source (Argonne National Laboratory), beamline 20-BM, for some experimental products. Uranium concentrations in fluids and solids after treatment were measured with inductively coupled plasma mass spectrometry (ICP-MS) (PerkinElmer SCIEX, ELAN DRC II, Department of Chemistry at MSU). After treatment, fluid and solid samples were collected from the hydrothermal reactor (autoclave). Approximately 10 mg of each solid sample were digested in 10 ml of 3% trace metal HNO_3. Fluid samples were collected and filtered with 0.45 μm nylon Whatman syringe filter. Standard solution of uranium (1000 ppm) was used to generate a calibration curve. All samples, fluids, and solids were diluted according to the initial U concentrations added to fall under the calibration curve generated. All dilutions, including standards, were prepared using 3% trace metal HNO_3 to maintain a homogenous matrix solution.

Table 1

Initial experimental conditions; confirmed mineralogy; U in solids and fluids (measured and calculated), and partitioning values using Nerst (D^U) and Doener-Hoskins ($K_{D-H}^{U/Ca}$).

Run	T °C	U(in) ppm	Bru. mg	A., Vol ml	Fl, Vol ml	pH 25 °C	pH_T	pH_T (calc)	XRD solids	U_{meas} Solids mol/kg	U_{meas}(fin) mol/kg	U(in) Calc. mol/kg	UO_2^{++} Calc.(in) mol/kg	Ca Calc. mol/kg	D^U(in)	D^U(fin)	D^U(in) UO_2^{++}	$K^{U/Ca}$ (D—H)
Y1	25	1	200	25	15	4.44	4.44	3.94	Monetite	7.92E-04	5.47E-09	4.20E-06	3.71E-06	1.29E-02	1.89E+02	1.45E+05	2.14E+02	7.20
Y2	25	1	200	25	15	4.48	4.48	3.94	Monetite	1.62E-04	8.69E-09	4.20E-06	3.71E-06	1.29E-02	3.85E+01	1.86E+04	4.36E+01	5.83
Y3	25	5	200	25	15	4.81	4.81	3.89	Monetite	2.69E-03	5.48E-07	2.10E-05	1.85E-05	1.47E-02	1.28E+02	4.90E+03	1.45E+02	7.11
Y4	25	5	200	25	15	5.32	5.32	3.89	Monetite	3.94E-03	6.82E-08	2.10E-05	1.85E-05	1.47E-02	1.88E+02	5.78E+04	2.13E+02	10.02
Y5	25	10	200	25	15	5.12	5.12	3.84	Monetite	6.29E-03	6.06E-08	4.20E-05	3.71E-05	1.69E-02	1.50E+02	1.04E+05	1.70E+02	9.44
Y6	25	10	200	25	15	5.08	5.08	3.84	Monetite	6.11E-03	6.19E-08	4.20E-05	3.71E-05	1.69E-02	1.45E+02	9.88E+04	1.65E+02	9.94
WB1	39	1	1000	900	800	4.9	4.99	4.7	Apatite	3.81E-03	7.31E-09	4.20E-06	3.01E-06	2.48E-03	9.06E+02	5.20E+05	1.27E+03	16.42
WB2	39	5	1000	900	800	4.8	4.89	4.52	Apatite	1.72E-02	6.22E-08	2.10E-05	1.59E-05	4.03E-03	8.21E+02	2.77E+05	1.09E+03	35.86
WB4	39	1	1000	900	800	5.02	5.1	4.7	Apatite	5.74E-03	8.69E-09	4.20E-06	3.01E-06	2.48E-03	1.37E+03	6.61E+05	1.91E+03	14.99
1C	80	0.04	203	100	60.23	4.31	4.3	3.91	Apatite	7.85E-05	2.41E-09	1.68E-07	1.14E-07	5.34E-03	4.67E+02	3.26E+04	6.91E+02	8.72
2C	80	0.1	248	100	60.58	4.38	4.37	3.87	Apatite	5.85E-04	6.67E-09	4.20E-07	2.87E-07	5.59E-03	1.39E+03	8.77E+04	2.03E+03	10.01
3C	80	0.3	200	100	61.02	4.59	3.58	3.92	Apatite	1.93E-04	2.92E-09	1.26E-06	8.51E-07	5.31E-03	1.53E+02	6.63E+04	2.27E+02	6.90
4C	80	0.6	211	100	60.82	4.45	4.44	3.88	Apatite	1.16E-03	6.18E-09	2.52E-06	1.72E-06	5.70E-03	4.59E+02	1.87E+05	6.74E+02	9.45
5C	80	1	207	100	60.47	4.78	4.77	3.88	Apatite	1.92E-03	2.48E-08	4.20E-06	2.86E-06	5.77E-03	4.56E+02	7.74E+04	6.70E+02	8.91
6C	80	10	208	100	61.62	4.48	4.47	3.78	Apatite	5.29E-03	7.22E-08	4.20E-05	2.91E-05	7.35E-03	1.26E+02	7.32E+04	1.82E+02	12.49
Z1	120	1	200	25	15.19	3.35	3.37	3.21	Mon-Ap	7.24E-04	4.69E-07	4.20E-06	2.48E-06	7.58E-03	1.72E+02	1.54E+03	2.92E+02	4.09
Z2	120	2	200	25	15.24	3.35	3.38	3.2	Mon-Ap	1.17E-03	4.94E-07	8.40E-06	4.96E-06	7.85E-03	1.39E+02	2.37E+03	2.36E+02	4.29
Z3	120	5	200	25	15.23	4.29	4.32	3.16	Mon-Ap	3.21E-03	2.51E-06	2.10E-05	1.25E-05	8.71E-03	1.53E+02	1.28E+03	2.58E+02	3.89
Z4	120	7	200	25	15.21	4.29	4.32	3.14	Mon-Ap	2.57E-03	2.65E-06	2.94E-05	1.75E-05	9.30E-03	8.74E+01	9.69E+02	1.47E+02	3.78
Z5	120	10	200	25	15.43	4.12	4.15	3.82	Mon-Ap	3.23E-03	2.67E-06	4.20E-05	2.50E-05	1.01E-02	7.68E+01	1.21E+03	1.29E+02	4.04
1CL	120	0.01	206	100	60.34	3.95	3.98	3.82	Apatite	4.32E-05	8.20E-10	4.20E-08	2.05E-08	2.75E-03	1.03E+03	5.27E+04	2.11E+03	5.80
2CL	120	0.02	213	100	60.83	3.88	3.91	3.78	Apatite	5.67E-05	6.34E-10	8.40E-08	4.17E-08	2.94E-03	6.75E+02	8.95E+04	1.36E+03	6.16
3CL	120	0.04	204	100	60.54	3.85	3.88	3.83	Apatite	7.98E-05	9.04E-10	1.68E-07	8.16E-08	2.73E-03	4.75E+02	8.83E+04	9.78E+02	6.06
4CL	120	0.1	204	100	61.28	3.84	3.87	3.83	Apatite	2.35E-04	1.22E-08	4.20E-07	2.04E-07	2.73E-03	5.60E+02	1.93E+04	1.15E+03	5.37
6CH	120	0.1	219	100	63.67	3.86	3.89	3.82	Apatite	2.36E-04	8.67E-09	4.20E-07	2.05E-07	2.80E-03	5.61E+02	2.72E+04	1.15E+03	5.60
5CL	120	0.3	201	100	60.96	3.82	3.85	3.82	Apatite	6.51E-04	1.13E-08	1.26E-06	6.13E-07	2.78E-03	5.16E+02	5.76E+04	1.06E+03	5.94
6CL	120	0.6	204	100	61.29	3.95	3.98	3.8	Apatite	1.67E-03	1.22E-08	2.52E-06	1.24E-06	2.92E-03	6.61E+02	1.36E+05	1.35E+03	6.71
1CH	120	1	207	100	60.68	3.91	3.94	3.77	Apatite	2.02E-03	2.45E-08	4.20E-06	2.10E-06	3.13E-03	4.80E+02	8.22E+04	9.63E+02	6.49
2CH	120	2	201	100	60.62	3.82	3.85	3.74	Apatite	4.30E-03	8.95E-08	8.40E-06	4.25E-06	3.44E-03	5.12E+02	4.81E+04	1.01E+03	6.68
3CH	120	5	210	100	62.73	3.75	3.78	3.62	Apatite	4.39E-03	1.30E-07	2.10E-05	1.11E-05	4.59E-03	2.09E+02	3.37E+04	3.95E+02	7.90
4CH	120	7	208	100	61.3	3.92	3.95	3.56	Apatite	5.13E-03	8.83E-08	2.94E-05	1.59E-05	5.37E-03	1.74E+02	5.80E+04	3.23E+02	8.96
5CH	120	10	208	100	60.52	3.86	3.89	3.48	Apatite	5.34E-03	1.16E-07	4.20E-05	2.31E-05	6.51E-03	1.27E+02	4.61E+04	2.31E+02	10.63
1B	160	0.04	200	50	30.36	3.15	3.21	3.38	Apatite	4.77E-05	4.18E-09	1.68E-07	2.05E-08	3.13E-03	2.84E+02	1.14E+04	7.37E+02	3.95
2B	160	0.1	202	50	30.58	3.22	3.29	3.37	Apatite	8.12E-05	1.30E-08	4.20E-07	6.47E-08	3.15E-03	1.93E+02	6.27E+03	5.01E+02	3.78
3B	160	0.3	203	50	31.85	3.19	3.25	3.38	Apatite	3.17E-04	9.86E-09	1.26E-06	1.62E-07	3.14E-03	2.52E+02	3.22E+04	6.55E+02	4.42
4B	160	0.6	196	50	30.36	3.18	3.24	3.37	Apatite	6.25E-04	1.61E-08	2.52E-06	4.84E-07	3.24E-03	2.48E+02	3.87E+04	6.43E+02	4.56
5B	160	1	199	50	30.44	3.24	3.31	3.35	Apatite	5.92E-04	5.67E-08	4.20E-06	9.73E-07	3.36E-03	1.41E+02	1.04E+04	3.63E+02	4.03
6B	160	10	204	50	30.57	3.3	3.39	3.16	Apatite	3.36E-03	2.06E-07	4.20E-05	1.63E-06	5.74E-03	8.00E+01	1.63E+04	1.97E+02	5.39
U-A	200	0.1	1	25	15	2.57	2.69	2.87	Mon-Ap	2.14E-04	2.70E-07	4.20E-07	1.26E-07	2.97E-03	5.10E+02	7.93E+02	1.70E+03	1.37
U-B	200	0.1	1	25	15	2.53	2.65	2.87	Mon-Ap	4.14E-04	3.11E-07	4.20E-07	1.26E-07	2.97E-03	9.86E+02	1.33E+03	3.30E+03	1.48
U-A1	200	1	1	25	15	2.85	2.97	2.86	Mon-Ap	1.98E-03	3.71E-06	4.20E-06	1.26E-06	3.01E-03	4.71E+02	5.34E+02	1.58E+03	1.24
U-B1	200	1	1	25	15	2.8	2.92	2.86	Mon-Ap	1.77E-03	1.58E-06	4.20E-06	1.26E-06	3.01E-03	4.22E+02	1.13E+03	1.41E+03	1.49
1CL	200	0.01	210	100	60.92	3.22	3.34	3.56	Apatite	1.61E-05	1.02E-09	4.20E-08	8.64E-09	1.38E-03	3.83E+02	1.58E+04	1.86E+03	3.89
2CL	200	0.02	222	100	60.04	3.26	3.38	3.54	Apatite	3.61E-05	6.50E-10	8.40E-08	1.75E-08	1.43E-03	4.30E+02	5.56E+04	2.06E+03	4.51
3CL	200	0.04	240	100	61.2	3.2	3.32	3.56	Apatite	7.17E-05	1.34E-09	1.68E-07	3.54E-08	1.48E-03	4.27E+02	5.37E+04	2.03E+03	4.44
4CL	200	0.1	220	100	60.21	3.25	3.37	3.56	Apatite	1.63E-04	2.26E-09	4.20E-07	8.75E-08	1.44E-03	3.87E+02	7.19E+04	1.86E+03	4.17
6CH	200	0.1	210	100	65.09	2.5	2.62	3.59	Apatite	3.24E-04	1.42E-08	4.20E-07	8.75E-08	1.36E-03	7.70E+02	2.27E+04	3.70E+03	4.61
5CL	200	0.3	260	100	60.35	3.44	3.56	3.48	Apatite	1.46E-03	1.77E-08	1.26E-06	2.70E-07	1.60E-03	1.16E+03	8.22E+04	5.39E+03	5.85
6CL	200	0.6	210	100	60.6	3.17	3.29	3.54	Apatite	4.31E-04	1.32E-08	2.52E-06	5.27E-07	1.52E-03	1.71E+02	3.26E+04	8.18E+02	4.02
1CH	200	1	230	100	61.02	3.31	3.43	3.49	Apatite	2.51E-03	1.16E-07	4.20E-06	8.97E-07	1.66E-03	5.97E+02	2.16E+04	2.80E+03	4.38
2CH	200	2	220	100	61.27	3.33	3.45	3.46	Apatite	5.64E-03	1.59E-07	8.40E-06	1.81E-06	1.86E-03	6.71E+02	3.54E+04	3.10E+03	4.98
3CH	200	5	210	100	61.39	3.34	3.46	3.36	Apatite	1.55E-02	1.67E-06	2.10E-05	4.70E-06	2.54E-03	7.38E+02	9.30E+03	3.30E+03	5.43

(*continued on next page*)

Table 1 (*continued*)

Run	T °C	U(in) ppm	Bru. mg	A., Vol ml	Fl, Vol ml	pH 25 °C	pH_T	pH_T (calc)	XRD solids	U_{meas} Solids mol/kg	U_{meas}(fin) mol/kg	U(in) Calc. mol/kg	UO_2^{2+} Calc.(in) mol/kg	Ca Calc. mol/kg	D^U(in)	D^U(fin)	D^U(in) UO_2^{++}	$K^{U/Ca}$ (D—H)
4CH	200	7	200	100	60.23	2.87	2.99	3.3	Apatite	1.53E-02	1.38E-06	2.94E-05	6.69E-06	3.03E-03	5.21E+02	1.11E+04	2.29E+03	5.43
5CH	200	10	200	100	62.77	2.33	2.45	3.23	Apatite	2.12E-02	9.58E-07	4.20E-05	9.73E-06	3.78E-03	5.05E+02	2.21E+04	2.18E+03	6.13
LANL1	200	1	200	25	10	2.69	2.81	3.08	Apatite	3.26E-04	2.55E-07	4.20E-06	1.06E-06	2.58E-03	7.75E+01	1.28E+03	3.07E+02	1.94
LANL2	200	1	200	25	10	2.44	2.56	3.08	Apatite	8.76E-04	1.84E-07	4.20E-06	1.06E-06	2.58E-03	2.08E+02	4.77E+03	8.19E+01	2.75
MSU1	200	10	200	25	10	2.81	2.93	2.98	Apatite	3.27E-03	1.29E-06	4.20E-05	1.07E-05	3.62E-03	7.79E+01	2.53E+03	3.06E+02	2.38
MSU2	200	10	200	25	10	2.65	2.77	2.98	Apatite	3.79E-03	4.36E-07	4.20E-05	1.07E-05	3.62E-03	9.02E+01	8.69E+03	3.54E+02	2.76
1C	220	0.04	218	100	60.24	3.72	3.81	3.55	Apatite	6.05E-05	1.73E-09	1.68E-07	2.49E-08	1.11E-03	3.60E+02	3.50E+04	2.43E+03	4.15
2C	220	0.1	213	100	60.25	3.83	3.98	3.56	Apatite	1.56E-04	6.78E-09	4.20E-07	6.20E-08	1.11E-03	3.71E+02	2.30E+04	2.52E+03	3.86
3C	220	0.3	211	100	60.5	3.93	4.09	3.55	Apatite	5.38E-04	1.05E-08	1.26E-06	1.87E-07	1.14E-03	4.27E+02	5.11E+04	2.88E+03	4.08
4C	220	0.6	217	100	60.57	3.96	4.11	3.53	Apatite	1.22E-03	1.23E-08	2.52E-06	3.77E-07	1.21E-03	4.84E+02	9.92E+04	3.23E+03	4.37
5C	220	1	217	100	61.7	3.65	3.8	3.51	Apatite	1.78E-03	5.67E-08	4.20E-06	6.33E-07	1.28E-03	4.23E+02	3.14E+04	2.81E+03	4.02
6C	220	10	226	100	60.77	3.46	3.62	3.2	Apatite	1.47E-02	6.08E-07	4.20E-05	6.93E-06	3.19E-03	3.50E+02	2.42E+04	2.12E+03	6.22
4C	350	0.1	25.4	40	10.2	2.97	3.99	4.04	Apatite	1.68E-04	1.85E-07	4.20E-07	8.22E-10	1.02E-04	4.00E+02	9.08E+02	2.05E+05	1.40
5C	350	1	36.4	40	10.2	2.88	3.9	4.04	Apatite	3.34E-04	1.01E-07	4.20E-06	8.48E-09	1.16E-04	7.95E+01	3.30E+03	3.94E+04	1.59
16C	350	25	32	40	10.2	2.66	3.68	3.97	Apatite	1.01E-02	2.20E-06	3.34E-05	6.68E-08	1.18E-04	9.82E+01	4.60E+03	1.51E+05	1.91

(*) Indicates experimental batch were conducted in a water bath (WB) using plastic containers instead of autoclaves. U(in) corresponds to uranium concentration adjusted by addition of U-aliquot; (Bru) is Brushite added to our system (mg); A., Vol indicates volume of the autoclave; Fl, Vol indicates amount of solution added to our system; $pH_{25\,°C}$ - pH measured at room temperature after experimental run. pH_T – temperature corrected pH; pH_T (calc.) - pH calculated via Gibbs free energy minimization. Thermodynamic calculations predicted apatite to be the only stable phase in all experiments. U_{meas} solids and U_{meas} (fin), are concentrations measured in solids and final fluids, respectively, via ICP-MS. U (in) Calc., total initial uranium in the system calculated (calculated using Gibbs free energy minimization) while UO_2^{++}(in) is uranyl ion concentration in the initial fluid corrected to uranyl fraction (Gibbs free energy minimization) Ca Calc. is Ca concentration in solutions calculated using Gibbs free energy minimization. D^U(in) indicates Nerst partitioning of U between solids and fluid calculated as U in solids over initial U added to our system. D^U(fin) indicates Nerst partitioning of U between solids and fluid calculated as U in solids over U measured in fluids. $D^U UO_2^{++}$ indicates partitioning of U between solids and fluid calculated as U in solids over uranyl ion concentration.

2.3. Thermodynamic calculations

Uranium (U) aqueous speciation and its total concentration in equilibrium with apatite were calculated by minimizing the Gibbs free energy under experimental conditions, such as solution composition, solid phase, oxygen fugacity, temperature, and saturated vapor pressure. Since aliquots of U standard solution with a matrix of 2% HNO_3 were used, the amount of mol of $UO_2(NO_3)_2$ was adjusted based on the initial amount added (i.e., 1 ppm = $4.20{\cdot}10^{-6}$ mol/kgH_2O). Subsequently, $5.5{\cdot}10^{-5}$ mol of HCl (for the case of 1 ppm of U), 0.5 mol of NaCl, and 1 kg of water were included in the calculations. The mol of brushite used in the calculations were determined from the amount of initial brushite and solution added (i.e., ~0.2 g of brushite in 60 ml of solution is equivalent to ~0.02 mol/kg of brushite).

The thermodynamic properties of water and its dissociation constant used in these calculations were from the Haar-Gallagher-Kell model (Kestin et al., 1984) and the Marshall and Franck model (Marshall and Franck, 1981), respectively. Aqueous complexes and their references were as follows: H^+, OH^-, O_2, H_2, Na^+, Ca^{2+}, CO_2, Cl^- (Johnson et al., 1992); NaOH, $CaCl^+$, $CaCl_2$, NaCl, $CaOH^+$ (Sverjensky et al., 1997); U^{3+}, U^{4+}, UO_2^+, UO_2^{2+}(Shock et al., 1997); UOH^{2+}, UO^+, UO_2^-, HUO_2, UO^{2+}, UOH^{3+}, UO_2OH, HUO_2^+, HUO_3^-, UO_3^-, UO_3, UO_4^{2-}, HUO_4^-, UO_2OH^+, UO_2 (Shock et al., 1997); SiO_2 (Shock and Helgeson, 1988); $H_3SiO_4^-$ (Busey and Mesmer, 1977); HCl (Tagirov et al., 1997); UCl_4 (Timofeev et al., 2018); $(UO_2)_2(OH)_2^{2+}$, $(UO_2)_2(OH)^{3+}$, $(UO_2)_3(OH)_4^{2+}$, $(UO_2)_3(OH)_5^+$, $(UO_2)_3(OH)_7^-$, $(UO_2)_4(OH)_7^+$ (Plyasunov and Grenthe, 1994); $NaCO_3^-$, $NaHCO_3$ (Smith and Martell, 1976); UO_2 (Guillaumont and Mompean, 2003); UO_2Cl_2, UO_2Cl^+ (Migdisov et al. (2018).

Since the thermodynamic data on aqueous speciation for uranium phosphate complexes at high temperatures are unknown, calculations were performed without phosphate complexes. Calculations with phosphate complexes (Shvarov and Bastrakov, 1999) yielded unrealistically high concentrations of dissolved uranium. The calculation used the extended Debye–Huckel model modified for NaCl-dominated solutions (Helgeson et al., 1981; Oelkers and Helgeson, 1990, 1991),

$$log\gamma_i = -\frac{A \bullet [Z_i]^2 \bullet \sqrt{I}}{1 + B \bullet \mathring{a} \cdot \sqrt{I}} + \Gamma + b_\gamma I \quad (1)$$

where γ_i is the activity coefficient of *i*, *A* and *B* are the Debye–Huckel parameters, Z_i, Γ, and $\mathring{a}$ are the individual molal activity coefficient, the charge, a molarity to molality conversion factor, and the distance of the closest approach of an ion *i*, respectively. *I* is the effective ionic strength calculated using the molal scale and b_γ is the extended-term parameter for NaCl-dominated solutions.

3. Results

3.1. Results for thermodynamic calculations

Results of calculations (pH_T) are presented in Table 1. All calculations yielded apatite as a solid phase. U concentrations (U_{total}) were controlled by setting it to U added as an aliquot and vary between $4.20{\cdot}10^{-8}$ to $4.20{\cdot}10^{-5}$ (mol of U per kg of H_2O). The predominant aqueous species of uranium were UO_2^{2+}, UO_3, UO_2Cl^+, UO_2OH^+, and UO_2Cl_2. As UO_2^{2+} has been previously suggested to be incorporated into apatite structure (Rakovan et al., 2002), it was used to evaluate partitioning along with total U concentration. The molar ratio of aqueous UO_2^{2+}/U_{total} strongly depended on temperature and decreased from 0.7 to 0.8 at 39 °C to 0.002 at 350 °C. No precipitation of U-rich phase was predicted with these calculations and apatite was the only solid phase in equilibrium with aqueous solution.

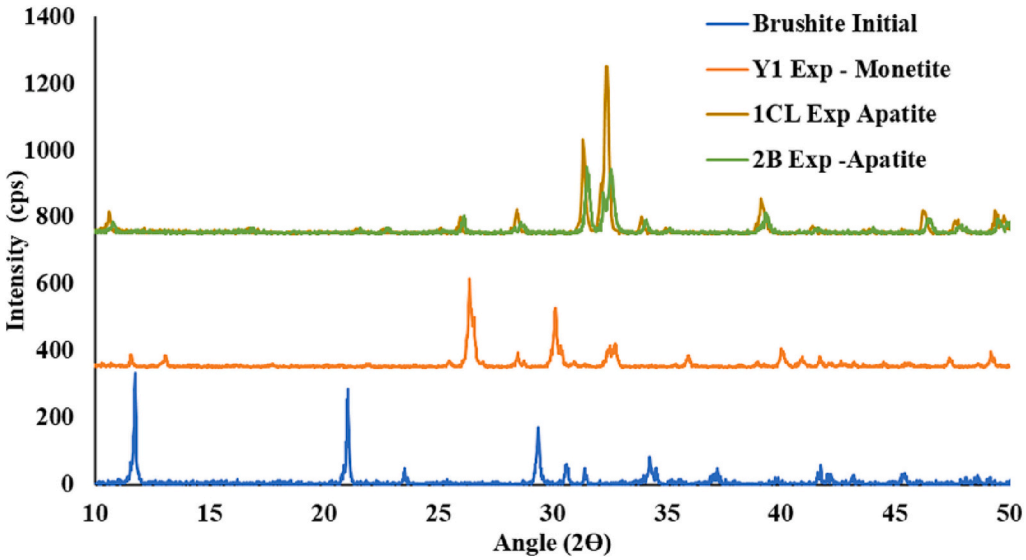

Fig. 2. XRD patterns of initial powder and mineral products: Initial brushite (blue), monetite (orange; Y1 experiment), and apatite (gold and green; 1CL and 2B experiments, respectively). (For interpretation of the references to colour in this figure legend, the reader is referred to the web version of this article.)

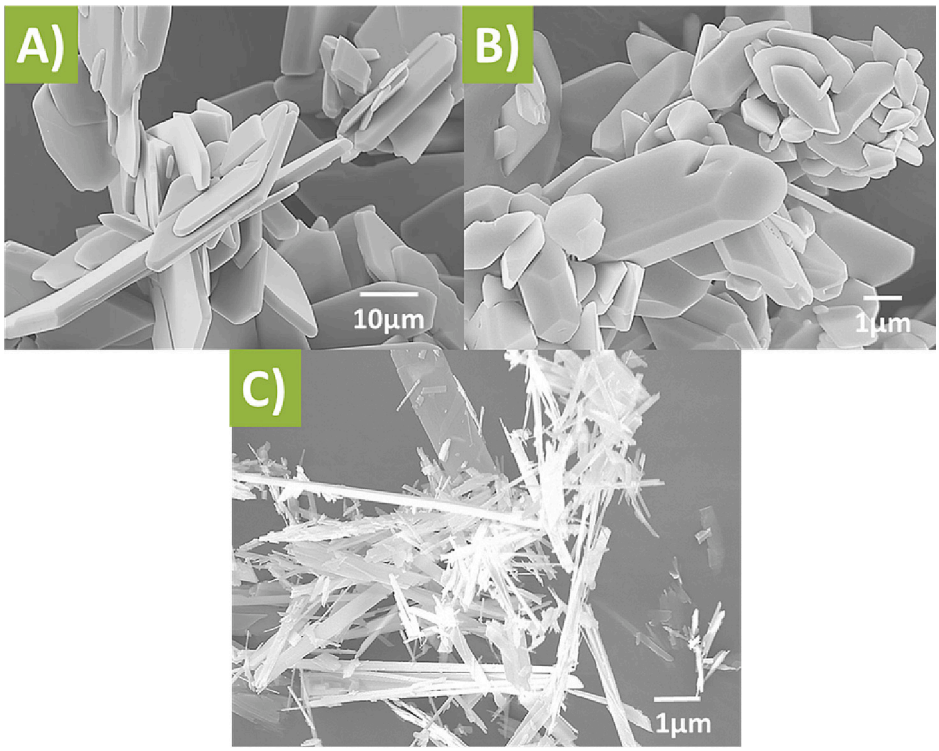

Fig. 3. SEM images showing the crystal morphology before and after experiments. A) Brushite: platy flower-like (before). B) Monetite: tabular (after; experiment that resulted in monetite). C) Apatite: acicular (after; experiments that resulted in apatite).

3.2. Results for sample characterization

XRD (Fig. 2) analyses confirmed that 100% brushite to apatite transformation was achieved in 52 out of 67 experiments. Experiments conducted at room temperature (n = 6) resulted in monetite, the anhydrous form of brushite. Other experiments (n = 9) conducted at 120 and 200 resulted in monetite-apatite mixtures. Imaging via SEM of experimental reactants and products yielded different morphologies. Fig. 3A is a representative SEM image of the initial brushite. Fig. 3B shows the monetite tabular morphology for reference. Fig. 3C, represents the brushite transformation into newly formed apatite. The morphology exhibits change from platy-flower like, to tabular, to acicular structure.

In XAFS analysis, the U L3-edge of samples 5CH and 2CH are relatively flatter than those in concentrated uranium oxide sample (in this case, dehydrated schoepite) due to the low U concentration (5CH: about 5000 ppm of U, 2CH: about 1000 ppm of U). For the samples having lower U concentration, we were not able to collect XAS spectra with a good quality. After obtaining the XAFS spectra in k^3-space (Fig. 4B), the spectra from both 5CH and 2CH have poor statistics in the high k region. Therefore, we focus our XAFS analysis on the first U—O coordination shells. The radial distribution function (RDF) of 5CH sample is visually

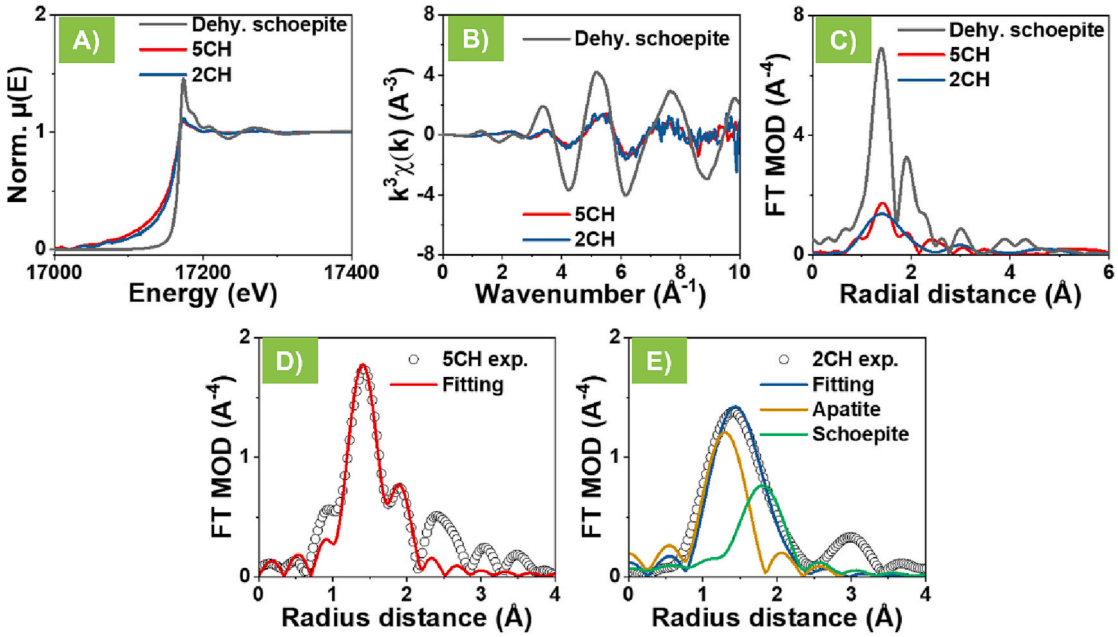

Fig. 4. XAS spectra of apatite samples (5CH and 2CH) indicating the presence of U^{6+}, in comparison of the schoepite spectrum from Finch et al. (1996) $[(UO_2)_8O_2(OH)_{12}](H_2O)_{12}$, in the energy space in A), k^3 space in B), with RDF spectra in C); D) the fitted XAFS spectrum of the product of experiment 5CH indicating schoepite; E) the fitted XAFS spectrum of the product of experiment 2CH indicating a mixture of schoepite and apatite.

Table 2
XAFS fitting results for sample 5CH and 2CH.

Sample	CN	R (Å)	σ ($\times 10^{-3}$ Å^2)	ΔE (eV)	Theor. CN	Theor. R (Å)	Phase
5CH	0.6 ± 0.0	1.80 ± 0.00	2.8 ± 0.6	8.1 ± 0.5	0.9	1.80	schoepite
	1.1 ± 0.1	2.31 ± 0.01	9.3 ± 1.1		0.8	2.30	schoepite
2CH	0.7 ± 0.0	1.80 ± 0.00	4.8 ± 0.6	5.7 ± 0.5	0.9	1.80	schoepite
	1.3 ± 0.1	2.32 ± 0.01	9.8 ± 1.0		3.0	2.40	apatite

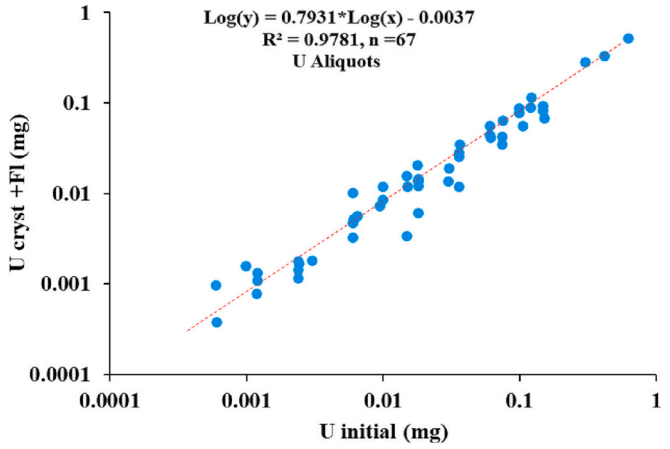

Fig. 5. Mass balance assessment of all experiments. U measured in crystal plus in the fluid versus U initial loaded to the autoclave.

similar to that of the dehydrated schoepite. In contrast, only one major peak was observed from the RDF curve of 2CH sample (see Fig. 4C). The XAFS fitting result suggests that the dominated form of U is schoepite in 5CH, and both U-incorporated apatite and schoepite in 2CH. Moreover, from the data, we derived the radial distances (Fig. 4B and C), which may shed light on lattice strain information regarding our experimental conditions and methods. For sample 5CH ($U_{fluid\text{-}initial}$ = 10 ppm, $U_{crystal}$ = 5045.20 ppm), two U—O paths from schoepite, 1.80 Å with 0.6 O atoms and 2.31 Å with 1.1 O atoms were observed (Fig. 4D and Table 2). Both paths are close to their theoretical locations (1.80 Å and 2.30 Å, respectively). For sample 2CH ($U_{fluid\text{-}initial}$ = 2 ppm, $U_{crystal}$ = 1341.18 ppm), two U—O scatterings are observed (Fig. 4E), with the first path corresponding to schoepite located at 1.80 Å, and the second path contributed from U-doped apatite phase located at 2.32 Å. It should be noted that due to the limited resolution of the XAFS data, the derivation of the phase ratio of schoepite and apatite was not feasible. Nevertheless, by using the XAFS data we were able to determine the uranium valence state and speciation in selected solids. Although XAS data suggested the presence of schoepite-like local structure features in both samples, crystallization of this phase was not predicted by thermodynamic calculation, nor was detected with XRD.

3.3. Uranium concentrations and partition coefficients

The controversial results were obtained in thermodynamic calculations and XAS of the high uranium samples crystallized at 200 °C (2CH and 5CH) where $U_{HAP} \geq 1342$ ppm and $U_{initial\ fluid} \geq 2$ ppm. There, no crystallization of U-rich minerals was predicted by calculations, but XAS data suggested crystallization of schoepite. Realizing that crystallization of uranium hydroxides would not be avoidable in the solutions where U ≥ 2 ppm, mass balance calculations were performed. Mass (in mg) of U dissolved in final solution was calculated as: $U_{fluid\text{-}measured}$ (ppm) · fluid volume (ml) / 1000 (ml). Mass (in mg) of U in apatite was calculated as: $U_{solid\text{-}measured}$ (ppm) · mass (g) / 1000 (g). Both were added (U_{fluid} [mg] + U_{solid} [mg]) and were compared with total amount of the initial U (in the aliquot) loaded into the autoclave. In the case of the precipitation of enriched-U phase, such as schoepite, which was heterogeneously dispersed within apatite and picked up for bulk analyses (ICP-MS), the

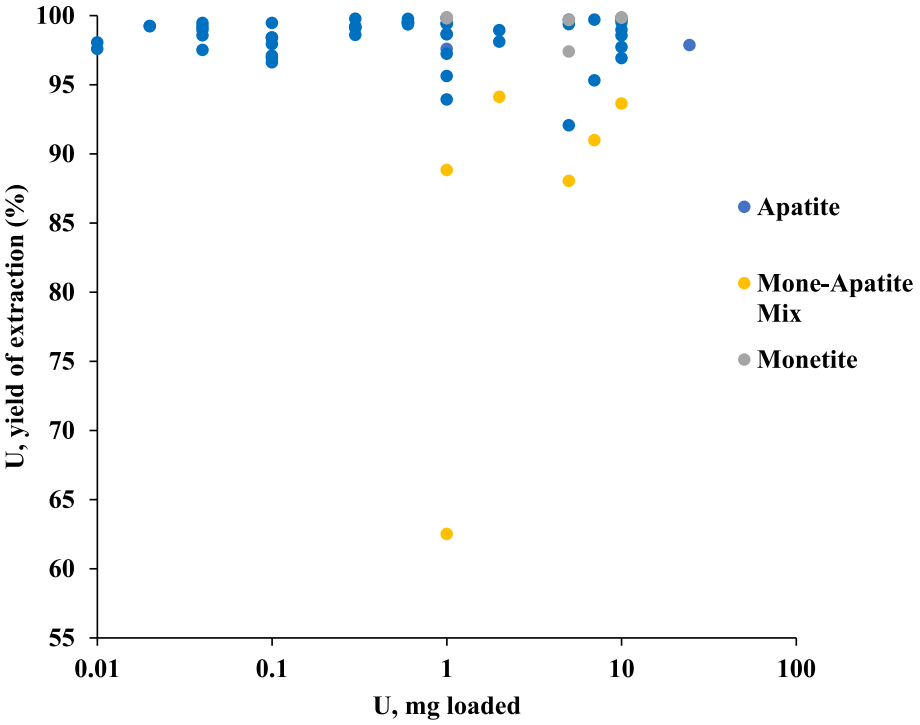

Fig. 6. U yield of extraction (%) versus U loaded to experiment (U aliquots experiments). Calculated as: 100% - [(U $_{\text{final fluid}}$ / U $_{\text{loaded}}$) *100]. The presented data is all temperatures, classified however, by resulting final mineralogy.

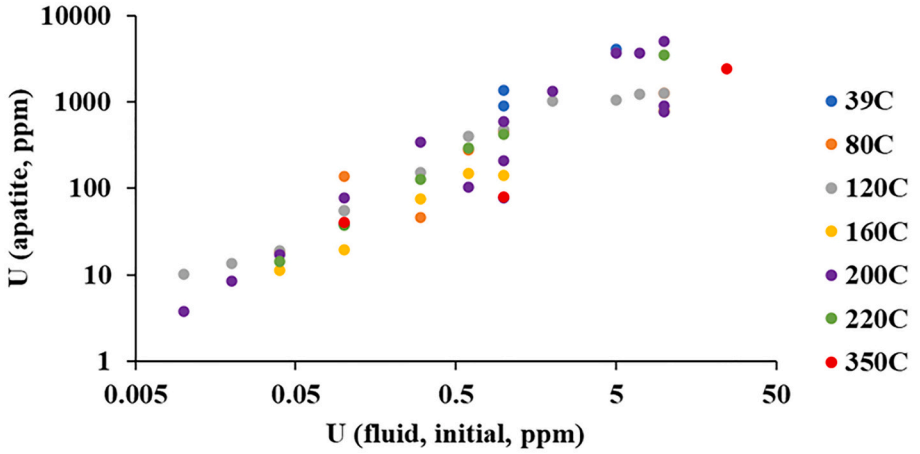

Fig. 7. U in apatite versus U initial in ppm. Increasing concentrations with increased initial U. Apparent saturation at 0.5 wt%.

mass balance assessment would have resulted in an overestimation of U measured. If heterogeneously dispersed schoepite was not picked up for ICP-MS analyses, then the mass balance assessment would have resulted in an underestimation of U measured. Our mass balance assessment shows no overestimation or underestimation of U in experiments with high uranium content (i.e., U > 0.1 mg); therefore, it is unlikely that U-enriched phases (i.e., schoepite) were picked up or excluded by bulk analysis unless nanocrystalline schoepite distributed homogeneously with apatite precipitate (Fig. 5).

The uranium yield of extraction was calculated as: 100% - [(U final fluid / U loaded) *100] and is represented in Fig. 6. In most of the experiments, apatite crystallization extracts >92% of dissolved uranium when a single mineral is achieved. Previous studies such as Moore et al. (2002, 2004) (and condensed in Rigali et al., 2016) showed that soils containing in-situ precipitated apatite decreased dissolved U by 89 to 99%, whereas dissolved U concentrations decreased by 62 to 91% in soils without the presence of apatite. Moreover, Arey et al. (1999) showed that the addition of hydroxyapatite to U-contaminated sediments (1703–2100 mg/kg U) reduced dissolved uranium concentrations to below the drinking water standard (30 mg/l), representing an ~98% removal of U. Monetite and apatite mixtures (120 °C), yielded an extraction percentage ranging from 65% to 86%. Although some experiments conducted at 200 °C resulted in monetite to apatite mixtures, all dissolved U was removed from solution. A plausible explanation could be that the amount initial brushite added to these experiments was approximately 5× more than that of regular experiments (1 g), allowing then, the entire removal of dissolved U. Monetite experiments yielded an extraction percentage of 99%. It should be noted that these experiments were conducted at room temperature with no additional treatment such as stirring, which could facilitate the transformation. Monetite has been identified as an effective mineral phase for the removal of dissolved U in a solution (Saghatchi et al., 2018) that coincides with our experimental

Table 3
Averaged partitioning data of U between crystal and fluid.

T (°C)	$K^{U/Ca}_{(D-H)}$ avg.	S.D.	Confirmed Mineralogy	1/TK*1000	Log ($K^{U/Ca}_{(D-H)}$)	S.D.	n
39	15.70	1.01	Apatite	3.20	1.20	0.03	2
80	8.80	1.17	Apatite	2.83	0.94	0.06	5
120	6.09	0.47	Apatite	2.54	0.78	0.03	9
160	4.15	0.33	Apatite	2.31	0.62	0.04	5
200	4.54	0.59	Apatite	2.11	0.66	0.06	9
220	4.09	0.19	Apatite	2.01	0.61	0.02	5
350	1.49	0.13	Apatite	1.61	0.17	0.04	2
200	1.39	0.12	Mone-Ap Mix	2.11	0.14	0.04	4
120	4.86	0.16	Mone-Ap Mix	2.54	0.69	0.01	2
25	6.52	0.97	Monetite	3.35	0.81	0.07	2
					Total		**45**

* The partitioning data is presented excluding experiments where $U_{fluid\text{-}initial} \geq 2$ ppm.

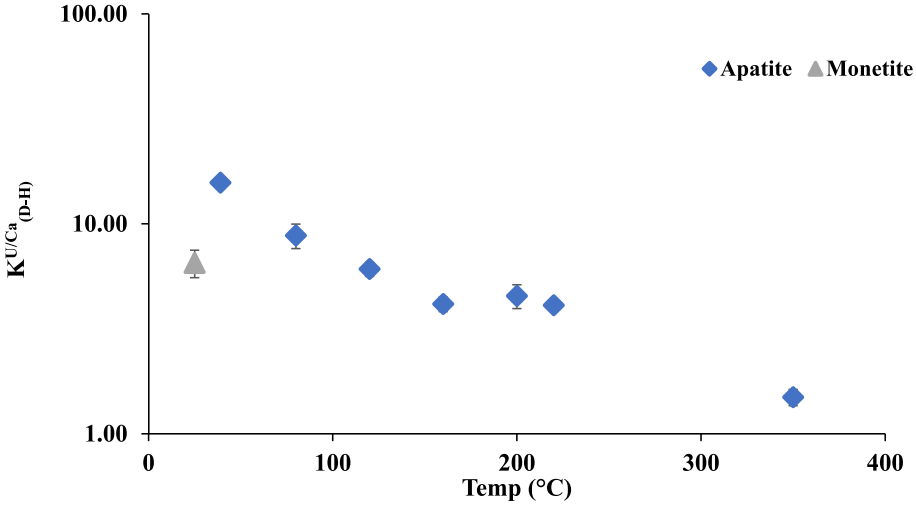

Fig. 8. Partition coefficients of uranium/calcium between mineral phase and fluid average by temperature. U partitioning aliquots experiments: apatite (blue diamond); monetite-apatite-mixture (orange square); monetite partitioning (gray triangle). (For interpretation of the references to colour in this figure legend, the reader is referred to the web version of this article.)

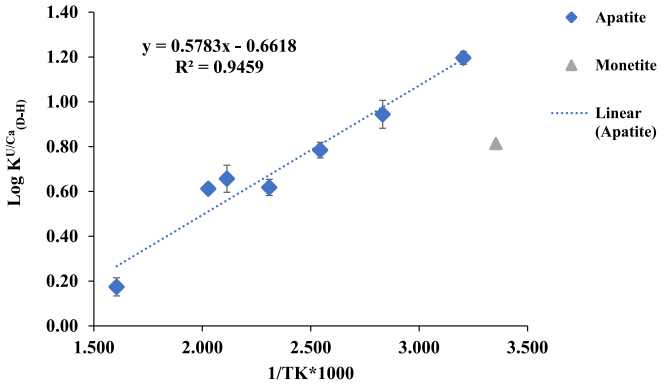

Fig. 9. $Log(K^{U}_{D-H})$ dependence on temperature of apatite crystallization.

data.

To evaluate a response of U uptake on its solution concentration, we plotted these data for different temperatures (Fig. 7), which showed that U in apatite is controlled by U added into solution when $U_{fluid} < 5$ ppm. These results are consistent with the ones reported in literature where authors reported dependency between U in solids and U added to solution, and the incorporation of U in biometric apatite increases proportionally as U in solution increases (Chatelain et al., 2015). However, at higher aqueous U concentrations (5, 7, and 10 ppm), U in apatite became independent on U in solution. This suggests: 1) schoepite can precipitate when aqueous uranium concentration exceeds 2 ppm; 2) apatite becomes saturated with uranium when $U_{apatite} \approx 0.5$ wt%. The first scenario is consistent with XAS observations but contradicts with thermodynamic calculations. All U aliquots experiments were conducted with an initial U concentration $\leq$ 10 ppm, to avoid the potential precipitation of uranium hydroxides phases. Overall, our results suggest the precipitation of schoepite is possible in our experiments where $U_{fluid} \geq 2$ ppm; therefore, partition coefficients evaluated from the experiments with high U content should be taken with caution. Because of this, experiments with $U_{fluid} \geq 2$ ppm were excluded from our calculations (i.e., D^{U}, $K^{U/Ca}_{D-H}$).

In most experiments a yield of extraction of >92% was achieved. Our values coincide with yield of extraction values reported in literature at lower temperature < 60 °C using hydroxyapatites (Skwarek et al., 2019). Demonstrating then, the ability of apatites to extract >92% of dissolved U at a wide range of temperatures.

Measured U concentrations in final fluids resulted in a decrease of 2–4 orders of magnitude than that of initial U loaded, demonstrating that all U was entrapped into newly formed apatites. Because of this, calculating of Nernst partition coefficients ($D^{U}=U_{apatite}/U_{solution}$) yielded vastly different (2–4 orders of magnitude) results while initial versus final U concentration in solution were used. Additionally, the Nernst partition coefficient does not provide information about the host,

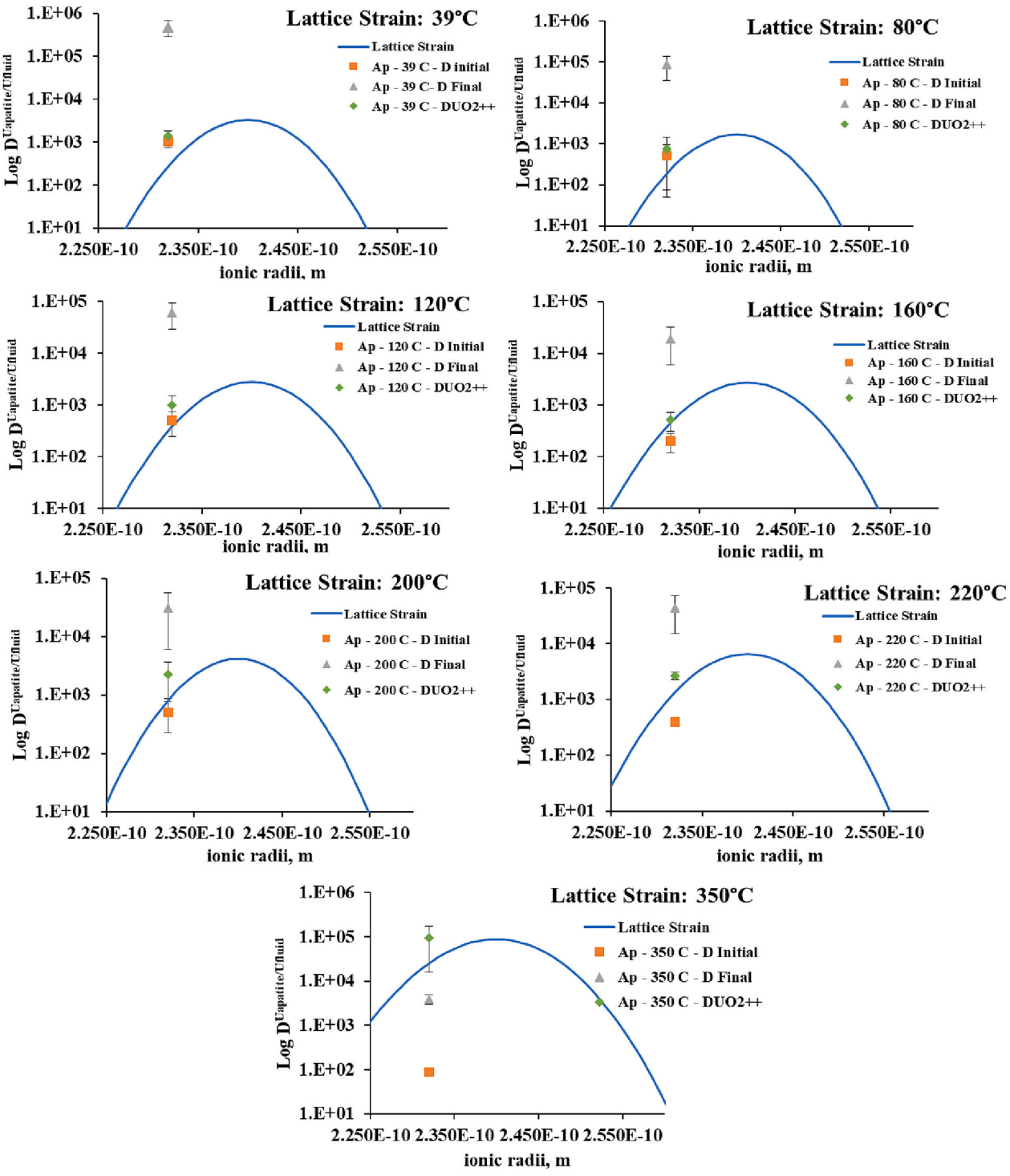

Fig. 10. Lattice Strains for $D^{Uapatite/Ufluid\text{-}initial}$ (orange), $D^{Uapatite/Ufluid\text{-}final}$ (gray) and $D^{Uapatite/Ufluid\text{-}UO2++}$ (green) values obtained in this study at experimental temperatures with the U—O path fixed at 2.32 Å obtained from XANES analysis. (For interpretation of the references to colour in this figure legend, the reader is referred to the web version of this article.)

calcium ion, which could potentially be replaced. In order to account for the change in U concentration during each experiment, modified Doener-Hoskins (D—H) equation (Doerner and Hoskins, 1925; Gaetani and Cohen, 2006) was applied for evaluating of U partition coefficient:

$$K_{D-H}^{U/Ca} = \frac{log\left(1+\frac{U_{crystal}}{U_{solution}}\right)}{log\left(1+\frac{Ca_{crystal}}{Ca_{solution}}\right)} \quad (2)$$

Here $Ca_{crystal}$ is concentration and total mass of Ca in the mineral phase (calculated using apatite or monetite stoichiometry, i.e., 0.078 mol and 0.216 mol, respectively). For experiments in which mineral phase mixture was achieved, the percentage of each mineral phase were obtained via XRD (i.e., 70% apatite and 30% monetite) and were used to calculate Ca via stoichiometry and corrected for the percentages. U_{Ap} and U_{sol} are total masses of U in apatite and final solution, respectively. However, authors suggest proceeding with caution when

Table 4
Thermodynamic parameters for uranium incorporation in apatite.

T°C	$Log\left(K_{D-H}^{U/Ca}\right)$	ΔG^0 (kJ/mol)	ΔH^0 (kJ/mol)	ΔS^0 (kJ/mol·K)
39	1.20	−3.10	−4.80	0.005
80	0.94	−2.77		
120	0.78	−2.56		
160	0.62	−2.23	E_a**(kJ/mol)**	
200	0.66	−2.58	From 39 to 350 °C	35.69
220	0.61	−2.51		
350	0.17	−0.90		

ΔG^0 and $Log\left(K_{D-H}^{U/Ca}\right)$ calculated. ΔH^0 and ΔS^0 were calculated from the slope and intercept (Fig. 9). E_a was derived from our data using Arrhenius equation.

calculating $K_{D-H}^{U/Ca}$ where mixture of mineral phases is achieved. Although we are presenting $K_{D-H}^{U/Ca}$ values for mineral mixture such values were excluded from further interpretation of data. Ca_{sol}^{*} and Ca_{sol} are calculated concentration and mass of Ca in solution. Calcium concentrations were calculated via Gibbs free energy minimization using HCH code and assumed to be constant during each experiment. Obtained values of $K_{D-H}^{U/Ca}$ vary from 1.24 to 16.42 and were independent from initial U added into our system. The values of $K_{D-H}^{U/Ca}$ were averaged for each temperature and included in Table 3. Fig. 8 shows a decrease of $K_{D-H}^{U/Ca}$ with increasing temperature. The temperature dependency suggests that at least near-equilibrium conditions were reached in our system. Therefore, $Log\left(K_{D-H}^{U/Ca}\right)$ values were plotted versus 1/TK*1000 to produce a plot and equation (Fig. 9) where the slope and intercept are equivalent to $-\frac{\Delta H^0}{RT}$ and $\frac{\Delta S^0}{R}$ respectively. Similarly, we derived ΔH° and ΔS° from this plot as followed: $\Delta H^\circ = -RT \cdot$ slope and $\Delta S^\circ = R \cdot$ intercept: (−4.80 kJ/mol and 0.005 kJ/mol·K, respectively).

4. Discussion

4.1. Uranium incorporation into apatite

We are presenting for the first-time uranium partitioning between apatite and fluid for a wide range of temperatures, which to our knowledge, has never been reported in the literature. U concentrations in our newly formed apatite minerals were approximately 3 orders of magnitude higher than that of U-aliquots loaded to experiment (i.e., 1 ppm loaded, 1000 ppm in apatite) and are dependent from the latter. However, it becomes independent when concentrations surpass 5 ppm of initial U loaded to experiment (Fig. 7). In addition to schoepite formation, this could indicate that U saturation in apatite with our experimental conditions is about 0.5 wt%. It is established in the literature that U content in igneous apatite makes up 0.001 to 0.01 wt%, around 0.005 to 0.02 wt% in sedimentary marine apatite, and it could be as high as 0.1 wt% in marine reworked apatite (Altschuler et al., 1958; Mortvedt, 1994). Our data show that U uptake by apatite was more effective at lower temperature and decreased with increasing temperature.

4.2. Lattice strain modeling

Although XAS spectra showed low resolution due to low U concentration, we were able to obtain preliminary radial distance information to attempt applying lattice strain model, which is based on crystallochemical properties of trace elements in minerals (Blundy and Wood, 1994). The lattice strain model equation used was:

$$D_i = D_o \bullet exp\left\{\frac{-4\pi E N_A \left[\frac{r_o}{2}(r_i - r_o)^2 + \frac{1}{3}(r_i - r_o)^3\right]}{RT}\right\} \quad (3)$$

where (r_i) is the ionic radius, (E) is Young's modulus, D_o is the strain-free partition coefficient for an element with ideal radius of r_o, N_A is Avogadro's number, R universal gas constant, and T, temperature is Kelvin. D_o was calculated using Ca in apatite (based on stoichiometry) and Ca in the fluid.

To compare our D^U values with those predicted with lattice strain model, we then, fixed our $D^{Uapatite/Ufluid\text{-}initial}$, $D^{Uapatite/Ufluid\text{-}final}$, and $D^{Uapatite/Ufluid\text{-}UO2^{++}}$ data to the U—O path obtained by XAS (2.32 Å) in apatite where U = 1342 ppm (2CH at 200 °C) (Fig. 10). This radial distance is significantly larger than those (2.06 Å) determined via XAS in apatite crystallized in non-aqueous system above 1000 °C (Rakovan et al., 2002). $D^{Uapatite/Ufluid\text{-}initial}$ was calculated as U measured in apatite over U added to our system. $D^{Uapatite/Ufluid\text{-}final}$ was calculated as U measured in apatite over U measured in the solutions. $D^{Uapatite/Ufluid\text{-}UO2^{++}}$ was calculated as U measured in apatite over a fraction of UO_2^{++} in the initial solutions calculated using Gibbs Free minimization Partition coefficients show an optimal correlation to the parabolic trend of the lattice strain model using radial distance of 2.32 Å. Our $D^U_{initial}$ values were in better consistency with lattice strain model in comparison to D^U_{final} and $D^{UO2^{++}}$ for all cases except for 350 °C. The relatively low values of $D^U_{initial}$ were because all species of U were considered in our system. Higher values of D^U_{final} were due to measured lower values of U in

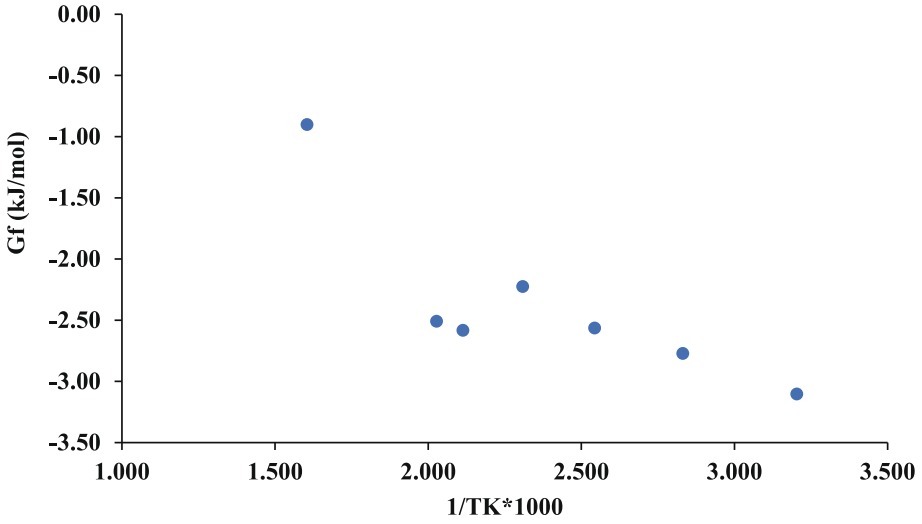

Fig. 11. Gibbs free energy of uranyl substitution reaction (ΔG^0) versus 1/TK*1000. ΔG^0 values obtained from this study (apatite only).

our fluids, indicating that all dissolved U was removed from solutions by apatite crystallization (observed as well with yield of extraction assessment). However, D^{U}_{final} was also considering all potential U species in our system. Contrary to $D^{U}_{initial}$ and D^{U}_{final}, D^{U} (UO_2^{++}) results from considering only UO_2^{++} species, which fraction decreases with increasing of temperature. Therefore, from 39 °C to 160 °C, it can be observed that $D^{U}_{initial}$ and D^{U} (UO_2^{++}) were similar or within analytical error. Subsequently from 200 °C to 220 °C, we can observe that D^{U} initial and D (UO_2^{++}) were different by an order of magnitude. This suggested that fraction of UO_2^{++} decreases with temperature, as larger discrepancies were observed between D^{U}_{final}, $D^{U}_{initial}$, and D(UO_2^{++}) at 350 °C. Comparison with lattice strain model suggested that knowledge of phosphate aqueous species at hydrothermal conditions could help to obtain more robust specie-dependent partition coefficient, i.e., other than D(UO_2^{++}).

4.3. Experimentally derived energies

Calculated Gibbs free energies of the exchange reaction for uranyl replacement of calcium in apatite are shown in Table 4 and Fig. 11, using $\Delta G^0 = -RTLog\left(K^{U/Ca}_{D-H}\right)$. $Log\left(K^{U/Ca}_{D-H}\right) = -\frac{\Delta H^0}{RT} + \frac{\Delta S^o}{R}$ where the slope is equivalent to $-\frac{\Delta H^0}{RT}$ and the intercept to $\frac{\Delta S^o}{R}$ (known as Van't Hoff plot) was used to extract ΔH° and ΔS° values. Since XAS data and lattice strain assessment provide sufficient evidence for ion exchange, the proposed formation reaction in this study is: $Ca_{ap} + UO_2^{2+} = UO_{2ap}^{2+} + Ca^{2+}$. Data suggests that products are favored over reactants at equilibrium at all temperatures where K > 1, Log K = positive and ΔG^0 = negative. Additionally, using the same plot we calculated activation energy (E_a) from $Log\left(\frac{K_1}{K_2}\right) = -\frac{Ea}{R} \bullet \left(\frac{1}{T_1} - \frac{1}{T_2}\right)$ (known as Arrhenius equation) where K_1 is $K^{U/Ca}_{D-H}$ at 39 °C and K_2 is $K^{U/Ca}_{D-H}$ at 350 °C. When considering temperatures from 39 to 350 °C, we obtained an activation energy of 35.69 kJ/mol, which is close to the value obtained by da Rocha et al. (2018) (42 kJ/mol). It should be noted that the values obtained by da Rocha et al. (2018) was for temperatures of 50, 55, and 60 °C, while this study evaluated a larger temperature range of 39 to 350 °C. Since da Rocha et al. (2018) evaluated the transformation from brushite to apatite (similar to this study) in KOH solutions (whereas this study NaCl) we find suitable the comparison between activation E_a. The comparison between E_a supports conventional knowledge that the reaction rate and/or partitioning decreases with increasing temperature. We realize that these assessments are only applicable for our experimental conditions. Future studies should evaluate the U entrapment from aqueous solutions where U = const using the brushite to apatite conversion method to provide accuracy on U entrapment, as well as to fill the temperature gap of this study (from 220 to 350 °C).

5. Conclusions

Experiments performed in this study demonstrate that apatite crystallization extracts >92% (average of 98%) of dissolved uranyl at a pH range from 3 to 4 at temperatures up to 350 °C. Our data suggests that uranyl uptake depends on temperature as values of Doener-Hoskins partition coefficient decreases from 15.7 to 1.5 while temperature increases from 39 to 350 °C. XAS analysis yielded the U—O radial distance in apatite of 2.32 Å, which is consistent with the lattice strain model. The combination of XAS, ICP-MS, and lattice strain modeling suggest that at 80, 160, 200, and 350 °C, U got incorporated into apatite at near-equilibrium conditions. An activation energy (E_a) of 35.69 (kJ/mol) has been obtained considering all temperatures, and this value is close to those reported in the literature (i.e., 42 kJ/mol; da Rocha et al., 2018). Experiments conducted at room temperature yielded transformation of brushite to monetite, where uranyl extraction exceeds 97%. Calculated average $K^{U/Ca}_{D-H}$ of 6.5 validates a potential of monetite for U incorporation.

Declaration of Competing Interest

The authors declare that they have no known competing financial interest or personal relationships that could have appeared to influence the work reported in this study.

Data availability

Data will be made available on request.

Acknowledgements

We thank the College of Arts and Sciences, Mississippi State University, for the funding provided through Strategic Research Initiative (SRI). We are also grateful for the support by the Nuclear Energy University Program (Department of Energy, DE-NE0009186, Project 21-23989). Research conducted at Los Alamos National Laboratory (LANL) was supported by the Laboratory Directed Research and Development (LDRD) program of LANL under project number 20180007DR. LANL, an affirmative action/equal opportunity employer, is managed by Triad National Security, LLC, for the National Nuclear Security Administration of the U.S. Department of Energy under contract 89233218CNA000001. A.S. also acknowledges the support of the G. T. Seaborg Institute through a Summer Research Fellowship at Los Alamos National Laboratory (LANL). Research at synchrotron conducted by Washington State University was supported by the National Science Foundation (NSF), Division of Earth Sciences, under award No. 2149848. This research used Beamline 20-BM of the Advanced Photon Source, a U.S. Department of Energy (DOE) Office of Science User Facility operated for the DOE Office of Science by Argonne National Laboratory under Contract No. DE-AC02-06CH11357, and the Canadian Light Source and its funding partners. We are grateful to Editor-in-Chief Karen Johannesson and two anonymous reviewers for their help with the improvement of the manuscript.

References

Altschuler, Z.S., Clarke, R.S., Young, E.J., 1958. Geochemistry of Uranium in Apatite and Phosphorite. U.S. Geological Survey Professional Paper 314-D.
Arey, J., Seaman, J.C., Bertsch, F.P., 1999. Immobilization of uranium in contaminated sediments by hydroxyapatite addition. Environ. Sci. Technol. 33, 337–342.
Blundy, J., Wood, B., 1994. Prediction of crystal–melt partition coefficients from elastic moduli. Nature 372 (6505), 452–454.
Busey, R.H., Mesmer, R.E., 1977. Ionization equilibriums of silicic acid and polysilicate formation in aqueous sodium chloride solutions to 300. Degree. C. Inorg. Chem. 16 (10), 2444–2450.
Carpéna, J., Audubert, F., Bernache, D., Boyer, L., Donazzon, B., Lacout, J.L., Senamaud, N., 1997. Apatitic waste forms: process overview. MRS Online Proce. Libr. Arch. 506.
Chatelain, G., Bourgeois, D., Ravaux, J., Averseng, O., Vidaud, C., Meyer, D., 2015. Incorporation of uranium into a biomimetic apatite: physicochemical and biological aspects. JBIC J. Biol. Inorg. Chem. 20 (3), 497–507.
Chaumont, J., Soulet, S., Krupa, J.C., Carpena, J., 2002. Competition between disorder creation and annealing in fluoroapatite nuclear waste forms. J. Nucl. Mater. 301 (2–3), 122–128.
Chew, D.M., Spikings, R.A., 2015. Geochronology and thermochronology using apatite: time and temperature, lower crust to surface. Elements 11 (3), 189–194.
da Rocha, D.N., da Silva, M.H.P., de Campos, J.B., Marçal, R.L.S.B., Mijares, D.Q., Coelho, P.G., Cruz, L.R., 2018. Kinetics of conversion of brushite coatings to hydroxyapatite in alkaline solution. J. Mater. Res. Technol.gy 7 (4), 479–486.
Doerner, H.A., Hoskins, W.M., 1925. Co-Precipitation of radium and barium sulfates1. J. Am. Chem. Soc. 47 (3), 662–675.
Ewing, R.C., Wang, Z., 2002. Phosphates as nuclear waste forms. Rev. Mineral. Geochem. 48, 673–699.
Finch, R.J., Cooper, M.A., Hawthorne, F.C., Ewing, R.C., 1996. The crystal structure of schoepite,[(UO 2) 8 O 2 (OH) 12](H 2 O) 12. Can. Mineral. 34 (5), 1071–1088.
Gaetani, G.A., Cohen, A.L., 2006. Element partitioning during precipitation of aragonite from seawater: a framework for understanding paleoproxies. Geochim. Cosmochim. Acta 70 (18), 4617–4634.
Gorman-Lewis, D., Shvareva, T., Kubatko, K., Burns, P., Wellman, D., McNamara, B., Szymanowski, J., Navrotsky, A., Fein, J.B., 2009. Thermodynamic properties of autunite, and uranyl orthophosphate from solubility and calorimetric measurements. Environ. Sci. Technol. 43, 7416–7422.

Greenburg, H.R., Wen, J., 2013. Repository layout and host rock thermal gradient trade study for large waste packages in clay/shale: Using the DSEF thermal analytical model. In: LLNL-TR-639869-DRAFT, p. 38.
Guillaumont, R., Mompean, F.J., 2003. Update on the Chemical Thermodynamics of Uranium, Neptunium, Plutonium, Americium, and Technetium, vol. 5. Elsevier, Amsterdam, pp. 64–70.
Helgeson, H.C., Kirkham, D.H., Flowers, G.C., 1981. Theoretical prediction of the thermodynamic behavior of aqueous electrolytes by high pressures and temperatures; IV, Calculation of activity coefficients, osmotic coefficients, and apparent molal and standard and relative partial molal properties to 600 degrees C and 5kb. Am. J. Sci. 281 (10), 1249–1516.
Hoeve, J., Sibbald, T.I.I., 1978. On the genesis of Rabbit Lake and other unconformity-type uranium deposits in northern Saskatchewan, Canada. Econ. Geogr. 73, 1450–1473.
Horie, K., Hidaka, H., Gauthier-Lafaye, F., 2008. Elemental distribution in apatite, titanate, and zircon during hydrothermal alteration: Durability of immobilization mineral phases for actinides. Phys. Chem. Earth 33, 962–968.
Hughes, J.M., 2015. The many facets of apatite. Am. Mineral. 100, 1033–1039.
Hughes, J.M., Rakovan, J., 2002. The crystal structure of apatite, Ca5 (PO4) 3 (F, OH, Cl). Rev. Mineral. Geochem. 48 (1), 1–12.
Jefferson, C.W., Thomas, D.J., Gandhi, S.S., Ramaekers, P., Delaney, G., Brisbin, D., Olson, R.A., 2007. Unconformity-associated uranium deposits of the Athabasca Basin, Saskatchewan, and Alberta. Bull. Geol. Surv. Can. 588, 23.
Johnson, J.W., Oelkers, E.H., Helgeson, H.C., 1992. SUPCRT92: a software package for calculating the standard molal thermodynamic properties of minerals, gases, aqueous species, and reactions from 1 to 5000 bar and 0 to 1000 C. Comput. Geosci. 18 (7), 899–947.
Kestin, J., Sengers, J.V., Kamgar-Parsi, B., Sengers, J.L., 1984. Thermophysical properties of fluid H2O. J. Phys. Chem. Ref. Data 13 (1), 175–183.
Marshall, W.L., Franck, E.U., 1981. Ion product of water substance, 0–1000 C, 1–10,000 bars New International Formulation and its background. J. Phys. Chem. Ref. Data 10 (2), 295–304.
Migdisov, A.A., Boukhalfa, H., Timofeev, A., Runde, W., Roback, R., Williams-Jones, A. E., 2018. A spectroscopic study of uranyl speciation in chloride-bearing solutions at temperatures up to 250 C. Geochim. Cosmochim. Acta 222, 130–145.
Migdisov, A., van Hartesveldt, N., Kalintsev, A., Nisbet, H., Xu, H., Caporuscio, F.A., Boukhalfa, H., Roback, R.C., Brugger, J., 2019. Re-visiting hydrothermal speciation of uranium. In: Goldschmidt Conference, Barcelona, 2019.
Moore, R.C., Holt, K., Sanchez, C., Zhao, H., Salas, F., Hasan, A., Lucero, D., 2002. In situ formation of apatite in soil and groundwater for containment of radionuclides and heavy metals. In: Sandia National Laboratories, SAND2002-3642.
Moore, R.C., Sanchez, C., Holt, K., Zhang, P., Xu, H., Choppin, G.R., 2004. Formation of hydroxyapatite in soils using calcium citrate and sodium phosphate for control of strontium migration. Radiochim. Acta 92 (9–11), 719–723.
Moreno, E.C., Varughese, K., 1981. Crystal growth of calcium apatites from dilute solutions. J. Cryst. Growth 53 (1), 20–30.
Mortvedt, J.J., 1994. Plant and soil relationships of uranium and thorium decay series radionuclides—a review. J. Environ. Qual. 23, 643–650.
Oelkers, E.H., Helgeson, H.C., 1990. Triple-ion anions and polynuclear complexing in supercritical electrolyte solutions. Geochim. Cosmochim. Acta 54 (3), 727–738.
Oelkers, E.H., Helgeson, H.C., 1991. Calculation of activity coefficients and degrees of formation of neutral ion pairs in supercritical electrolyte solutions. Geochim. Cosmochim. Acta 55 (5), 1235–1251.
Plyasunov, A.V., Grenthe, I., 1994. The temperature dependence of stability constants for the formation of polynuclear cationic complexes. Geochim. Cosmochim. Acta 58 (17), 3561–3582.
Rakovan, J., Reeder, R.J., Elzinga, E.J., Cherniak, D.J., Tait, C.D., Morris, D.E., 2002. Structural characterization of U (VI) in apatite by X-ray absorption spectroscopy. Environ. Sci. Technol. 36 (14), 3114–3117.
Rigali, M.J., Brady, P.V., Moore, R.C., 2016. Radionuclide removal by apatite. Am. Mineral. 101 (12), 2611–2619.
Romberger, S.B., 1984. Transport and deposition of uranium in hydrothermal systems at temperatures up to 300 C: geological implications. In: Uranium Geochemistry, Mineralogy, Geology, Exploration, and Resources, pp. 12–17.
Saghatchi, H., Ansari, R., Mousavi, H.Z., 2018. Highly efficient adsorptive removal of uranyl ions from aqueous solutions using dicalcium phosphate nanoparticles as a superabsorbent. Nucl. Eng. Technol. 50 (7), 1112–1119.
Shock, E.L., Helgeson, H.C., 1988. Calculation of the thermodynamic and transport properties of aqueous species at high pressures and temperatures: Correlation algorithms for ionic species and equation of state predictions to 5 kb and 1000 C. Geochim. Cosmochim. Acta 52 (8), 2009–2036.
Shock, E.L., Sassani, D.C., Willis, M., Sverjensky, D.A., 1997. Inorganic species in geologic fluids: correlations among standard molal thermodynamic properties of aqueous ions and hydroxide complexes. Geochim. Cosmochim. Acta 61 (5), 907–950.
Shvarov, Y.V., Bastrakov, E.N., 1999. HCh, A Software Package for Geochemical Equilibrium Modeling: User's Guide. Record 1999/25.
Skwarek, E., Gładysz-Płaska, A., Choromańska, J.B., Broda, E., 2019. Adsorption of uranium ions on nano-hydroxyapatite and modified by ca and Ag ions. Adsorption 25 (3), 639–647.
Smith, R.M., Martell, A.E., 1976. Critical Stability Constants: Inorganic Complexes, vol. 4. Plenum Press, New York, pp. 96–103.
Soulet, S., Carpéna, J., Chaumont, J., Krupa, J.C., Ruault, M.O., 2001. Determination of the defect creation mechanism in the mono-silicated fluoroapatite. Disorder modeling under repository conditions. J. Nucl. Mater. 299 (3), 227–234.
Sverjensky, D.A., Shock, E.L., Helgeson, H.C., 1997. Prediction of the thermodynamic properties of aqueous metal complexes to 1000 C and 5 kb. Geochim. Cosmochim. Acta 61 (7), 1359–1412.
Tagirov, B.R., Zotov, A.V., Akinfiev, N.N., 1997. Experimental study of dissociation of HCl from 350 to 500° C and from 500 to 2500 bars: Thermodynamic properties of HCl°(aq). Geochim. Cosmochim. Acta 61 (20), 4267–4280.
Timofeev, A., Migdisov, A.A., Williams-Jones, A.E., Roback, R., Nelson, A.T., Xu, H., 2018. Uranium transport in acidic brines under reducing conditions. Nat. Commun. 9 (1), 1–7.
Wright, J., Conca, J., 2002. Remediation of groundwater contaminated with Zn, Pb and Cd using a permeable reactive barrier with Apatite II. In RTDF PRB Action MeetingNov (Vol. 6, No. 7).